

CHEMICAL PHYSICS

High-field pulsed EPR spectroscopy under magic angle spinning

Orit Nir-Arad¹, Alexander B. Fialkov¹, David H. Shlomi¹, Nurit Manukovsky¹, Frederic Mentink-Vigier², Iliia Kaminker^{1*}

In this work, we demonstrate the first pulsed electron paramagnetic resonance (EPR) experiments performed under magic angle spinning (MAS) at high magnetic field. Unlike nuclear magnetic resonance (NMR) and dynamic nuclear polarization (DNP), commonly performed at high magnetic fields and under MAS to maximize sensitivity and resolution, EPR is usually measured at low magnetic fields and, with the exception of the Spiess group work in the late 1990s, never under MAS, due to great instrumental challenges. This hampers the investigation of DNP mechanisms, in which electron spin dynamics play a central role, because no experimental data about the latter under DNP-characteristic conditions are available. We hereby present our dedicated, homebuilt MAS-EPR probehead and show the pulsed MAS-EPR spectra of P1 center diamond defect recorded at 7 tesla. Our results reveal unique effects of MAS on EPR line shape, intensity, and signal dephasing. Time-domain simulations reproduce the observed changes in the line shapes and the trends in the signal intensity.

INTRODUCTION

Electron paramagnetic resonance (EPR) is a spectroscopic technique that probes the electronic structure of atoms, molecules, and materials around the unpaired electrons. It is based on the electronic Zeeman effect, where the degeneracy of the unpaired electron spin eigenstates is lifted under the presence of an external magnetic field. At the resonance condition, the energy difference between the eigenstates is matched by the energy of the applied electromagnetic radiation, and an EPR signal is observed. That resonance frequency informs about the local environment of the unpaired electron, which, in turn, provides information on the electronic structure of the system under investigation. EPR applications include probing of radicals, transition metals, and electronic defects in chemistry, biology, and material science.

High-field (>7 T) EPR offers advantages such as increased sensitivity, increased *g*-tensor resolution, reduced overlap of nuclear spin frequencies in hyperfine spectroscopy EPR experiments, and reduced linewidth of the central transition in half-integer high-spin systems (1–3). Despite these advantages, now most EPR spectrometers operate at magnetic fields ranging between 0.3 and 3 T. This is because high-field EPR poses numerous instrumental challenges: As the field increases, so does the required radiation frequency. Between 0.3 T (corresponding to ~9 GHz) and 3.5 T (~95 GHz) and, mostly, between 3.5 and 7 T (~200 GHz), the performance of many components is strongly degraded. Above 7 T, many characteristic EPR components are unavailable. While the passive components can be replaced by clever quasi-optical analogs (4–6), the absence of sources and amplifiers constantly hampers the development of high-field EPR. In particular, the limited power available at millimeter-wave frequencies affects the development of pulsed EPR, which requires higher instantaneous power; thus, most high-field EPR spectrometers are continuous-wave (CW). Now, whereas commercial low/medium-field EPR spectrometers are abundant, most high-field EPR spectrometers are homebuilt (7–20).

The scarcity of high-field pulse EPR instruments affects the implementation of high-field EPR, as well as the development of dynamic nuclear polarization (DNP) at high field. DNP is a ubiquitous method for signal enhancement in nuclear magnetic resonance (NMR), which has revolutionized solid-state NMR (ssNMR) allowing for applications previously deemed impossible (21). At the core of the DNP experiment lies the polarization transfer from unpaired electron spins to nuclear ones (21–26). The underlying mechanisms for DNP are still incompletely understood, and their analysis requires the inclusion of various time-domain properties of the electron spins, available only by pulsed EPR, preferably under identical conditions to the DNP experiment, because many of these properties are conditions dependent (26–36). At low fields (0.3 to 1.5 T), the high-power technology for electron spin manipulation is well established, and multiple advanced DNP experiments are being developed (37–40). At 3.3 and 7 T, EPR experiments have yielded important insights on the static solid (28, 41–43) and liquid Overhauser (44, 45) DNP mechanisms.

Still, most DNP-NMR is carried out at high field, under which pulse EPR data are nearly unavailable. Moreover, DNP-ssNMR is almost exclusively carried out under magic angle spinning (MAS), where the sample is subject to a fast rotation along an axis tilted by $\theta_m = \arccos(1/\sqrt{3}) \approx 54.74^\circ$ with respect to the magnetic field. MAS partially averages out anisotropic interactions, allowing for high-resolution ssNMR spectra (46, 47). The corresponding high-field MAS-EPR experiments have never been carried out, leaving the understanding of MAS-DNP to rely on theoretical considerations (25, 26) and elaborate numerical simulations (48–52). The only pulsed MAS-EPR experiments were carried out under low field (0.3 T) in the late 1990s (53, 54), as were the related right-angle spinning (RAS)-EPR experiments (55–57). Two noteworthy recent reports include (i) a theoretical study, which focused on the observable effects in ultrahigh-speed MAS-EPR at $\nu_r > 150$ kHz and high fields (58), and (ii) a demonstration of CW EPR under MAS in a custom-built DNP/EPR probehead at 7 T (59). Still, the pulsed MAS-EPR experiments were never followed up; thus, despite the progress in static high-field EPR (2, 12, 60, 61), high-field pulsed MAS-EPR was never developed.

Copyright © 2024 The Authors, some rights reserved; exclusive licensee American Association for the Advancement of Science. No claim to original U.S. Government Works. Distributed under a Creative Commons Attribution NonCommercial License 4.0 (CC BY-NC).

¹School of Chemistry, Tel-Aviv University, 6997801 Tel-Aviv, Israel. ²National High Magnetic Field Laboratory, Florida State University, Tallahassee, FL 32310, USA.

*Corresponding author. Email: iliakam@tauex.tau.ac.il

Over the past years, we constructed a dual high-field DNP/EPR spectrometer, operating either in CW (62) or in pulse mode (63). Having imparted MAS abilities to it, we present here the first high-field (7 T) pulsed EPR spectra acquired under MAS. Here, we first describe the design of the homebuilt MAS-EPR probehead. Then, MAS-EPR spectra and time-domain measurements are presented, revealing unique effects that are absent in static EPR spectra. Last, numerical simulations are used to reproduce the experimental observations.

RESULTS

MAS-EPR probehead

We constructed a dedicated DNP/EPR probehead to enable the MAS-EPR experiments. A photograph of the probehead is shown on Fig. 1A, and the computer-assisted design (CAD) cutout of the probehead and the spinning module on Fig. 1 (B and C), respectively. The spinning module is based on the spherical rotor design introduced and developed by the Barnes group (64–67).

The design challenge in the MAS-EPR probehead design is to ensure minimal losses and high efficiency of millimeter-wave coupling to the sample spinning at few kilohertz. We optimized the probe for induction mode EPR detection, where the sample is excited with linearly polarized millimeter waves and the signal is detected at the orthogonal polarization (12); thus, our design ensured that both polarizations propagate efficiently.

In the DNP/EPR spectrometer in our laboratory, the millimeter-wave radiation is generated by a 450-mW solid-state source. The beam propagates as a free-space Gaussian beam with a ~8-mm beam waist through the quasi-optical table positioned below the magnet and then enters the probe from the bottom (Fig. 1B). The beam is coupled to the bottom of the smooth-wall waveguide taper with an output diameter of 5 mm, which reduces the beam size. After leaving the taper, the millimeter waves pass through the high-density polyethylene (HDPE) stator and the polytetrafluoroethylene (PTFE) spherical rotor to reach the sample. The spherical rotors have an 8-mm outer diameter and were machined from Grade 10 PTFE bearing balls (Precision Plastic Ball Company, IL USA), by drilling a hole of 2-mm diameter to the depth of ~6 mm. The sample, a powder, was packed into the hole that was sealed with a three-dimensionally (3D) printed plug.

To avoid high losses, which are detrimental to the EPR experiments sensitivity, the materials used in the parts of the probehead lying on the millimeter-wave beam path, the stator and the rotor, were carefully selected. For example, resin-based 3D printed stators that were used in the initial stages of the MAS-EPR probehead design have limited transparency compared to computer numerical control-machined HDPE stator used in the final version. Similarly, zirconia spherical rotors that have good spinning characteristics (up to 10 kHz) result in a sixfold reduction in EPR signal intensity due to the high loss tangent and high refractive index, resulting in high Fresnel reflections from the rotor (68–70) (see the Supplementary Materials). Both HDPE and PTFE plastics have a low refractive index and a very low loss tangent at the 200-GHz frequency, thereby facilitating the EPR detection. In addition, the radio frequency (rf) coil is positioned in such a way as not to interfere with the millimeter-wave beam. CAD files with the design of the stator and the stator holder are available in the Supplementary Materials. The magic angle is roughly set by the design of the gas flow in the stator (64), and the fine adjustment is done mechanically by tilting the stator holder. A single gas flow is used for rotor spinning (64). The stator includes fiber optic connections for optical readout of the spinning frequency. The rf circuit was tuned to 74.1 MHz, the ^{13}C frequency at 6.9 T. The ^{79}Br signal from the KBr powder was used to verify the magic angle adjustment as described in the Supplementary Materials. Note that the rf coil was present, although not used, in the MAS-EPR experiments described here.

MAS-EPR spectra

Echo-detected EPR spectra for different MAS frequencies are shown in Fig. 2A. The limited output millimeter-wave power leads to selective pulses (900-ns pulses were used to acquire the spectra in Fig. 2A) that excite only a small part of the EPR spectrum. The spectra are thus acquired by stepping the frequency throughout the EPR spectrum while plotting the magnitude of the echo at each point. This is a key aspect of the effects described below. The static spectrum, shown in black, is characteristic of the P1 center (substitutional nitrogen) defect in diamonds. The P1 center is a spin $S = 1/2$ defect that occurs when a single nitrogen atom substitutes for a carbon in the diamond lattice. The spectrum is dominated by the hyperfine interaction of the electron with an $I = 1$ ^{14}N nuclear spin. The principal values for the ^{14}N hyperfine interactions are 81.3, 81.3,

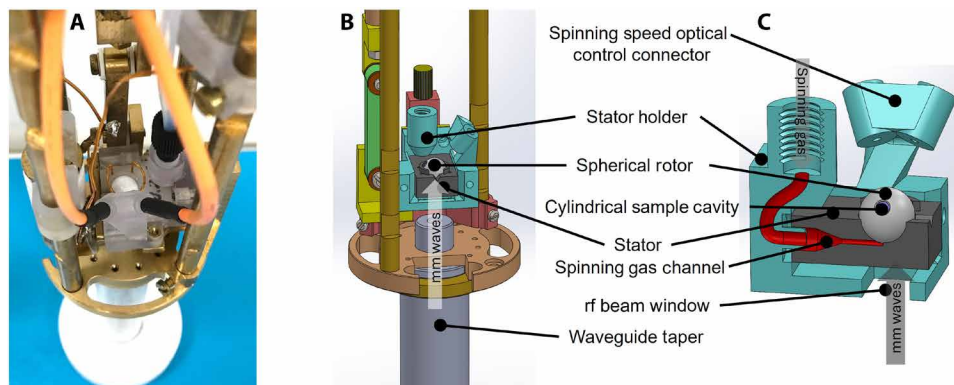


Fig. 1. The MAS-EPR probehead. (A) The photograph and (B) CAD cutout of the MAS-EPR probehead. (C) A detailed cutout of the spinning module assembly. The stator and the stator holder are cut in the plane of the spinning gas stream. mm waves, millimeter waves.

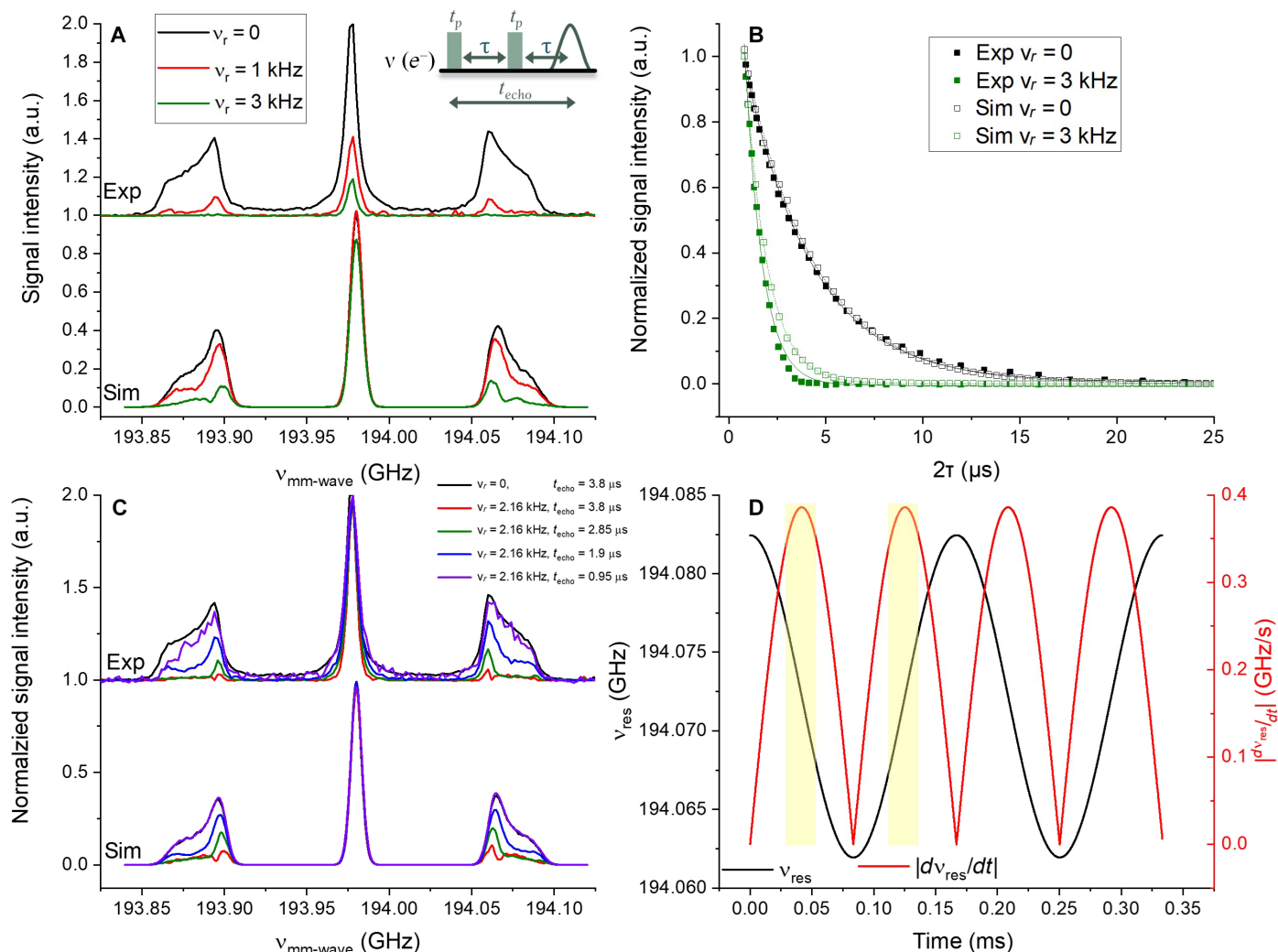


Fig. 2. MAS-EPR results. (A) Frequency swept pulsed EPR spectra of P1 centers in diamond powder as a function of the MAS frequency (ν_r). Top line, experimental spectra; bottom line, simulation. All experimental/simulated spectra are normalized by the maximum intensity of the experimental/simulated static spectra, respectively. $t_{\text{echo}} = 2.85 \mu\text{s}$, $t_{\text{rep}} = 5 \text{ ms}$. (B) Comparison of static and spinning two-pulse echo decays of the central ($m_I = 0$) line. Solid symbols, experimental data; open symbols, simulation; lines, exponential fit. All four datasets are normalized by their individual maximum intensities. $t_p = 1.2 \mu\text{s}$, $t_{\text{rep}} = 2.5 \text{ ms}$. (C) Changes in the EPR line shape as a function of the pulse sequence length for $\nu_r = 2.16 \text{ kHz}$. Top line, experimental spectra; bottom line, simulation. All 10 spectra are normalized by their individual maximum intensities. Experimental parameters: $t_{\text{echo}} = 3.8 \mu\text{s}$: $t_p = 1.2 \mu\text{s}$, $\tau = 700 \text{ ns}$; $t_{\text{echo}} = 2.85 \mu\text{s}$: $t_p = 900 \text{ ns}$, $\tau = 525 \text{ ns}$; $t_{\text{echo}} = 1.9 \mu\text{s}$: $t_p = 600 \text{ ns}$, $\tau = 350 \text{ ns}$; $t_{\text{echo}} = 0.95 \mu\text{s}$: $t_p = 300 \text{ ns}$, $\tau = 175 \text{ ns}$; $t_{\text{rep}} = 5 \text{ ms}$. (D) Simulated resonance frequency ν_{res} of a single spin packet belonging to the $m_I = +1$ manifold (black) and absolute value of its time derivative $\left| \frac{d\nu_{\text{res}}}{dt} \right|$ (red) as a function of time for $\nu_r = 3 \text{ kHz}$. The yellow vertical bars denote the region with the highest change in resonance frequency, which results in the highest distortion in the MAS-EPR spectrum. a.u., arbitrary units.

and 114.0 MHz (71). The two powder patterns on the left and the right of the EPR spectrum correspond to the $m_I = 1$ and $m_I = -1$ ^{14}N spin states, respectively. The sharp central line corresponds to the $m_I = 0$ ^{14}N spin state and is not subject to the hyperfine interaction. The powder patterns of the $m_I = \pm 1$ transitions are due to the anisotropic e - ^{14}N dipolar coupling. Thus, the resonance frequency in the $m_I = \pm 1$ manifolds depends on the orientation of the e - ^{14}N vector relative to the magnetic field, B_0 , which yields two Pake-like lines separated by the isotropic hyperfine interaction.

Upon sample spinning, the EPR spectrum undergoes marked changes. At the spinning frequency of 1 kHz, the EPR signal intensity is substantially reduced for all the transitions. However, the effect is more pronounced for $m_I = \pm 1$ transitions, where the signal

reduction is stronger and a line shape distortion is observed. Upon further increase of the spinning frequency to 3 kHz, the $m_I = \pm 1$ transitions practically disappear, and the signal intensity of the central transition drops to $\sim 1/5$ of its original intensity. Sample spinning results in a change in the orientation of the hyperfine tensor relative to the magnetic field and, thus, in a change in the resonance frequency of the electron spin. When the sample is static, the first pulse of the echo pulse sequence (inset in Fig. 2A) excites a subset of the spin packets, and, then, a second pulse refocuses the same spin packets whose resonance frequencies are constant over time forming an echo (72). In contrast, upon spinning the sample, the phase and frequency of all spin packets in the powder pattern have changed during the interpulse delay. In this case, the selective nature of the

pulses prevents full refocusing by the echo pulse sequence. The faster the sample reorientation, the fewer spin packets are refocused by the echo sequence, resulting in the signal reduction with increase of the MAS frequency. Such orientation dependence of the resonance frequency is much smaller for the central $m_I = 0$ transition, where, in the absence of the hyperfine interaction, the only source of the orientation dependence is the modest dependence of $g(t)$ upon sample spinning due to small g -anisotropy, which prevents full refocusing of the echo. The intensity of the central ($m_I = 0$) transition is thus affected by the MAS to a much lesser extent compared to the $m_I = \pm 1$ transitions. This dephasing is reflected in the decrease of the phase memory time from $T_m = 3.5 \mu\text{s}$ in the static experiment to $T_m = 0.9 \mu\text{s}$ for the sample spinning at 3 kHz (Fig. 2B); both were fitted with a monoexponential function.

To further understand the nature of the line shape distortion and intensity decrease observed with MAS, we performed numerical simulations of the MAS-EPR experiment, using an $S = 1/2$, $I = 1$ system, as in the experiment, and the same magnetic tensors. The simulated MAS-EPR spectra presented in Fig. 2A reproduce well the line shape change but underestimate the intensity decrease upon spinning. The remaining discrepancy is attributed to the presence of additional unresolved electron-electron dipolar couplings (63, 73), which we did not take into account in the simulations. Because the dipolar interaction is anisotropic, it will serve as an additional dephasing mechanism. We note that the experimental static spectrum shows a nonzero intensity between the three main lines, whereas the simulated one does not. The reason for this is the presence of exchange-coupled P1 center clusters in the diamond (63), which we excluded from the simulation. It should thus be noted that sample spinning has an additional effect of removing the broad component observed in the static spectrum, which also contributes to the discrepancy between the experimental and simulated signal reduction upon MAS. The disappearance of this broad component is attributed to the presence of strong dipolar interactions, the anisotropy of which is responsible for the rapid dephasing of this broad component upon MAS. Thus, MAS can serve to distinguish between overlapping signals based on their different anisotropies. The simulation also reproduces the increased dephasing of the central $m_I = 0$ manifold upon spinning (Fig. 2B); again, the extent of the MAS induced dephasing is underestimated with simulated $T_m = 1.15 \mu\text{s}$ (compared to experimental of $0.9 \mu\text{s}$), which is attributed to the e-e dipolar interactions that we did not take into account in the simulations.

The EPR spectra line shape of the $m_I = \pm 1$ transitions can be partially recovered by shortening the length of the pulse sequence (t_{echo} in the inset in Fig. 2A). Figure 2C (top) shows the change in the EPR spectral line shape with reduction of the echo time for MAS frequency of 2.16 kHz. Expectedly, the spectra acquired with long echo times are strongly distorted. Shortening the echo time allows for complete recovery of the EPR line shape, albeit at the expense of reduced signal-to-noise ratio due to the reduced flip angle of the shorter millimeter-wave pulses. The shorter the pulse sequence, the smaller the frequency shift due to MAS and the better the refocusing becomes, thus restoring the line shape. The simulation accurately captures this trend (Fig. 2C, bottom). The slight variations in signal intensity throughout the experimental spectrum, which are not captured by the simulations, are due to the variations in the millimeter-wave source power output with frequency and the presence of standing waves in the quasi-optical bridge.

The strongest reduction in the MAS-EPR signal intensity in the middle of the $m_I = \pm 1$ powder patterns and smaller effect at the canonical orientations (Fig. 2, A and C) can be understood by considering the rate of the change in the resonance frequency of the electron spin with MAS. A trajectory of a resonance frequency $\nu_{\text{res}}(t)$ of a single spin packet belonging to the $m_I = 1$ manifold at 3-kHz spinning frequency is shown on Fig. 2D in black overlaid with absolute value of its time derivative $\left| \frac{d\nu_{\text{res}}}{dt} \right|$ in red. We expect that the EPR signal will be the least affected by MAS where $\left| \frac{d\nu_{\text{res}}}{dt} \right|$ is the smallest. This is the case: The $\left| \frac{d\nu_{\text{res}}}{dt} \right|$ is the smallest around the g_{\perp} and g_{\parallel} where it reaches zero. The maximum of the $\left| \frac{d\nu_{\text{res}}}{dt} \right|$ occurs in the center of the powder pattern (marked by yellow rectangles on Fig. 2D) away from the canonical orientations, and, therefore, the pulsed EPR signal reduction is maximal in this region.

Echo shapes under MAS

Examples of the time-domain EPR echo traces are presented in Fig. 3. They were acquired at the central ($m_I = 0$) line and on the maximum of the $m_I = 1$ powder pattern. The exact spectral positions are indicated in the MAS-EPR spectrum in the inset. The echo of the central line acquired under MAS has a similar shape as the one acquired under static conditions. Still, it has a weaker intensity, its maximum is shifted to an earlier time, and its width is smaller. The same effects are much more pronounced in the echoes acquired within $m_I = 1$ powder pattern. The signal intensity is reduced further, the maximum of the echo is shifted to even earlier times, and the width is narrower. The reduced echo intensities, especially at later times, result from the dephasing and the shift of the resonance frequencies associated with the change in the electron spin resonance frequency. As expected, they are more pronounced for the $m_I = 1$ compared to $m_I = 0$ due to the faster change in the resonance frequency with MAS for the former. The same data presented with the simulated echo traces normalized to the intensity of the corresponding experimental ones is presented in fig. S3.

The simulated echo shapes, width, timing, and relative intensity reproduce the trends observed in the experimental ones. The static echo has its recognizable shape, while the echoes observed under MAS are much smaller, shifted to earlier times and narrower.

Repetition time

Unlike in most MAS-NMR where, typically, the whole spectrum is excited, the pulses in EPR experiments are selective; while, in static pulsed EPR experiments, where a pulse sequence repeatedly applied at a given frequency affects the same spin packets, under MAS, each subsequent pulse sequence affects a different spin packet that becomes on resonance at that instant due to MAS. This allows for a much faster pulsed EPR signal accumulation compared to the static case where a delay of $> T_{1e} \sim 1.5 \text{ ms}$ is used to allow for the recovery of the magnetization. While the reduction of signal intensity due to saturation is clearly visible for the static pulsed EPR spectrum (Fig. 4, topmost traces), it is absent from the MAS-EPR spectra, and the spectra acquired with 50- μs and 5-ms repetition time are identical (bottom traces). Thus, much faster signal averaging is possible for the MAS-EPR spectra, partially offsetting the reduced signal intensity necessitated by using low flip-angle pulses. The ability for fast signal averaging was previously discussed in the RAS experiments at low field (74), and we note that similar benefits are obtained by

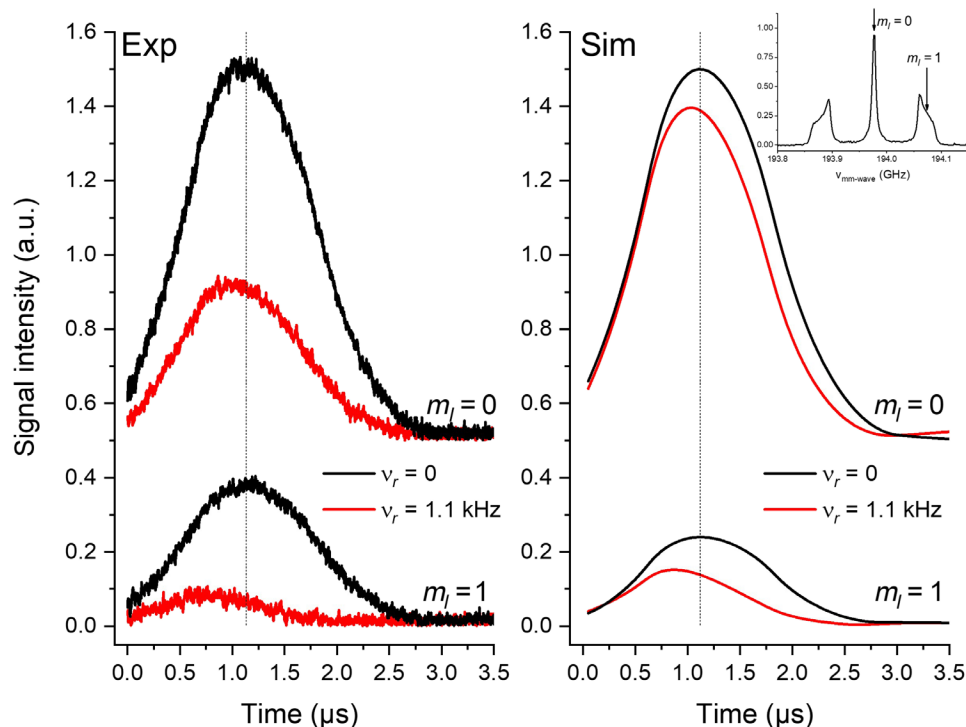


Fig. 3. Echo shapes. Comparison of the static and spinning experimental transient traces acquired in magnitude mode for the central line and the middle of the $m_l = 1$ powder pattern. The spectral positions where each of the echo traces was acquired are indicated with arrows in the spectrum presented in the inset. The experimental parameters were as follows: $t_{p1} = t_{p2} = 1.2 \mu\text{s}$; $\tau = 0.7 \mu\text{s}$; repetition time, 5 ms; a 16-step phase cycling with 50 averages per step was applied, $\nu_r = 1 \text{ kHz}$.

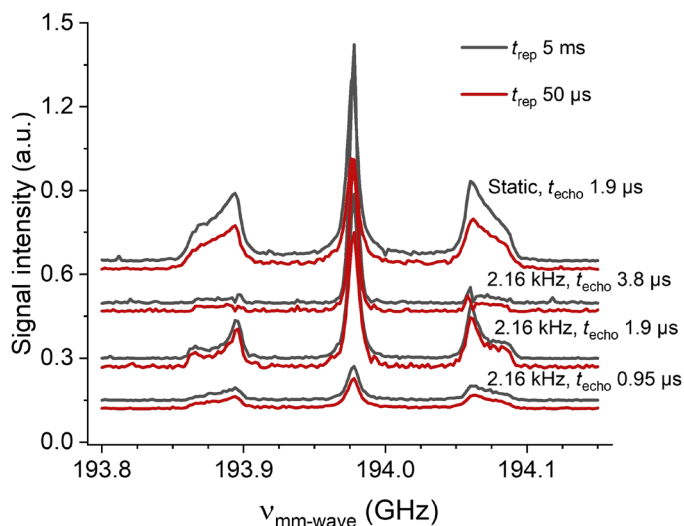


Fig. 4. MAS-EPR results. Comparison of the pulsed EPR spectra acquired with 5- and 50- μs repetition times for static and MAS with $\nu_r = 2.16\text{-kHz}$ pulsed EPR spectra. Other experimental parameters appear in the caption of Fig. 2C.

using field jumps to acquire multiple pulsed EPR experiments in parallel (75).

Experimental determination of the ν_1 frequency in the spinning sample

The ability to perform pulsed EPR experiments with the MAS-DNP probehead allowed us to experimentally determine the efficiency of

millimeter-wave delivery to the sample by measuring the electron nutation frequency, $\nu_1 = \omega_1/2\pi$. This ability has great practical importance for the DNP probehead development. A massive effort is invested in high-power millimeter-wave sources and optimization of the probehead design to facilitate the millimeter-wave delivery to the sample, because the strength of the electron nutation frequency is crucial for saturation of the electron spins and the success of the DNP experiment (76, 77). Figure 5 shows the experimental three-pulse echo-detected nutation experiment recorded with the MAS-EPR probehead. The nutation experiment was recorded under static conditions on the central $m_l = 0$ line. The experimental trace was fitted with a damped cosine function (solid line in Fig. 5), and the nutation frequency $\nu_1 \sim 180 \text{ kHz}$ was extracted from this fit. The experimentally obtained value is higher than the one obtained from simulations by the Barnes group (77), similar to the one calculated by the Griffin group (76), and lower than the estimated ones by the Bruker team for their probes (78). While an analogous nutation experiment can be carried out under MAS (fig. S4), its interpretation is not straightforward because the nutation pulse and the pulses forming the echo no longer affect the same spin packets.

DISCUSSION

In this work, we report the first high-field pulsed EPR spectra in spinning samples. We were able to observe the time domain evolution of the electron spins under MAS at high magnetic fields, revealing effects such as the line shape distortion and the faster decoherence caused by MAS. Simulations reproduce the changes in line shapes and echo shapes observed in the experiments and thus aid in clarifying

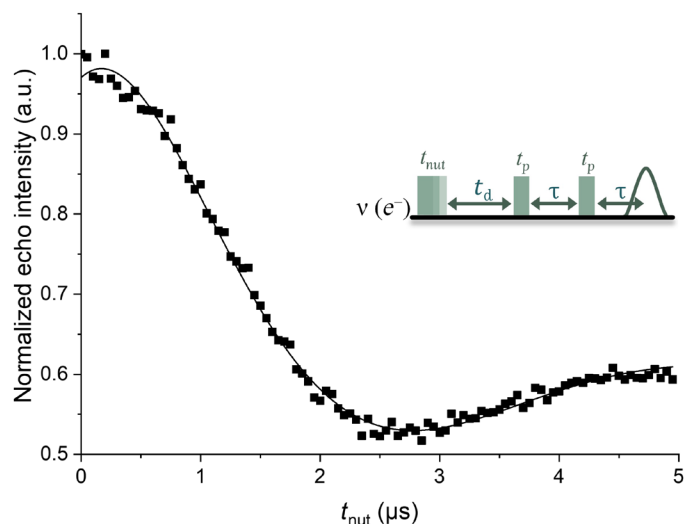


Fig. 5. Nutation experiment. The three-pulse nutation experiment performed on the P1 center defects in diamond powder using MAS-EPR probehead. The solid line is a fit using a damped cosine function to extract the nutation frequency.

the source of the former phenomena. We attribute the success of the pulsed EPR experiments presented here to the probehead design that allows for propagation of the two orthogonal polarization modes and for the efficient millimeter-wave penetration that we achieved by the material choice of HDPE and PTFE for the stator and the rotor, respectively, with both plastics having a very low loss tangent and small refractive indices at the millimeter-wave frequencies. In addition, in the presented design, the rf coil is positioned such as not to interfere with the millimeter-wave beam path.

These experiments open the possibility for the long sought after observation of the electron spin dynamics under MAS at high field for the investigation of DNP. One of the most useful experiments for the investigation of static DNP mechanisms is the electron-electron double resonance experiment. This is a pump probe experiment that allows for probing the effect of prolonged millimeter-wave irradiation, typical of DNP, on the electron spins (27–30). We envision its MAS-EPR analog to be extremely useful in the investigation of MAS-DNP mechanisms. Accessing the regime typical of contemporary DNP experiments will require the development of a cryogenic MAS-EPR probehead capable of MAS-EPR experiments at ≤ 100 K.

Further developments would include rotor-synchronized pulsed EPR; while in MAS-NMR rotor-synchronized sequences, where the pulses are repeated in multiples or a constant fractions of a rotor period are very common, their analogy is not possible in MAS-EPR, because all the electron coherences decay in the fraction of the rotor period due to the short electron T_2 . Still, experiments such as stimulated echo, where the magnetization is stored along the z direction and thus decays with T_1 timescale, should be possible in the future, when MAS-EPR with faster spinning is developed. The slower decay of the longitudinal magnetization will allow for rotor-synchronized sequences where the EPR signal will be refocused following the return of the rotor to its original orientation. The original MAS-EPR work used similar ideas (53) borrowed from NMR (79). This will require an order-of-magnitude increase in the spinning speed, which is well within the capabilities of the current MAS technology. In addition, the increase in EPR relaxation times at lower temperatures

characteristic of DNP will further facilitate the rotor-synchronized MAS-EPR experiments when the relevant experimental capabilities ($\nu_r \approx 40$ kHz, $T \leq 100$ K) are developed. To reach the “true MAS-NMR” regime will require not only >1 -MHz spinning speeds but also hundreds of MHz electron spin nutation frequencies (58). While tens of MHz nutation frequencies are possible when high millimeter-wave power is combined with high-quality factor (high-Q) resonance structures (80, 81), implementation of high-Q resonance structures compatible with MAS remains a challenge.

We envision that further development of MAS-EPR hardware and methodology may lead to EPR experiments with enhanced resolution. The method can be used to simplify spectra by separating broad and narrow components of overlapping EPR spectra such that the signal with the larger anisotropy disappears while the one with the smaller is still observable. In addition, this can be further applied to yield high-resolution electron-nuclear double resonance experiments where small interactions, amenable to averaging with modern >100 -kHz spinning speed MAS, are resolved.

MATERIALS AND METHODS

The DNP/EPR spectrometer

We performed the MAS-EPR experiments using the homebuilt DNP/EPR spectrometer recently constructed in Tel-Aviv University (62). For pulsed EPR experiments, we modified the spectrometer by the addition of a pulse-forming unit, allowing for phase adjustment and pulse slicing of the CW microwave to generate the pulses at ~ 16 GHz. The pulse-forming unit is equipped with an arbitrary waveform generator (AWG), allowing for the generation of microwave pulses with an arbitrary phase. The pulse durations and the phases are set in the ~ 16 -GHz pulse-forming unit (the phases are set to 1/12th of their target phase at 200 GHz, to account for subsequent frequency multiplication). The microwave pulses are fed into the high-power (~ 0.5 W) $\times 12$ amplifier multiplier chain (Virginia Diodes Inc.), which outputs the desired millimeter-wave pulse sequence with correct phases and pulse durations.

The detection is achieved using a superheterodyne scheme with the downconverted in-phase and quadrature (I and Q) signals being digitized using a fast (3 giga sample/sec) two-channel digitizer (Vitretek LLC). This scheme allows for a phase sensitive detection and, together with AWG capabilities of the pulse forming unit, for full phase cycling capabilities. The DNP/EPR spectrometer uses induction mode EPR detection where the electron spins are excited using linearly polarized millimeter waves. The circularly polarized EPR signal is detected at the polarization orthogonal to the one used for excitation. This scheme, known as inductive detection, facilitates isolation between the transmitting and receiving parts of the spectrometer and allows for the use of high-power pulses that would, otherwise, damage the receiver (12). Induction mode detection requires that both orthogonal modes can efficiently propagate through all the millimeter-wave pathways. We constructed the MAS-EPR probehead with this requirement in mind. The detailed description of the pulsed EPR operation of the DNP/EPR spectrometer will be published elsewhere.

MAS-EPR spectra

The MAS-EPR spectra were recorded using a Hahn Echo pulse sequence (inset in Fig. 2A) with two pulses of the same length (t_p) and a delay (τ) between them. The echo signal appears approximately at

time τ after the second pulse. The EPR spectra were recorded by stepping the millimeter-wave frequency. A 16-step phase cycling $\phi_{p1} = [0^\circ, 90^\circ, 180^\circ, 270^\circ]_4$, $\phi_{p2} = [0^\circ, 90^\circ, 180^\circ, 270^\circ]_4$, and $\phi_{\text{detection}} = \phi_{p1} - 2\phi_{p2}$, where subscript 4 refers to the four consecutive repetitions for the pulse/block of pulses, was applied to remove the contributions of the free induction decays from both pulses and mixer imperfections. The EPR spectra were obtained by integrating over the full width at half maximum of the echo signal in the magnitude mode. The pulse and delay lengths are given in the figure captions.

We performed a measurement of the millimeter-wave B_1 field strength with the three-pulse nutation experiment using a $t_{\text{nut}} - t_d - t_p - \tau - t_p - \tau - \text{echo}$ sequence (inset in Fig. 5). The same 16-step phase cycle as in the echo detected EPR spectra was used for the last two pulses; $\phi_{\text{nut}} = 0^\circ$; $t_d = 10 \mu\text{s}$, $t_p = 1.2 \mu\text{s}$, and $\tau = 700 \text{ ns}$ were used. The repetition time was 2 ms, and 150 shots per point were recorded.

$B_0 = 6.92202 \text{ T}$ for the experiments presented in the Results section; all experiments were carried out at room temperature.

Sample

The sample used for EPR experiment was an HPHT diamond powder with consistent but irregular crystal shapes with a particle size around $44 \mu\text{m}$, purchased from Element Six UK Ltd. (PDA657 325400 D46). The P1 center concentration in this sample is ~ 120 parts per million as determined by spin counting on a CW X-band Bruker Elexsys E500 spectrometer.

Simulations

We performed simulations using a home-written MATLAB (MathWorks) code. The spin system considered was a single electron spin $1/2$ with g -anisotropy coupled to a ^{14}N nuclear spin. The experimental g -tensor [$g_{\perp} = 2.0020$; $g_{\parallel} = 2.0018$] and hyperfine tensor [$A_{\perp} = 2\pi \times 81.3 \text{ MHz}$; $A_{\parallel} = 2\pi \times 114 \text{ MHz}$] were used and assumed to be colinear. The calculations were carried out in the rotating frame of the electron spin, and we considered the simple Hamiltonian

$$\hat{H}(t) = [g(t)\mu_B B_0 - \omega_{\text{mw}}] \hat{S}_z + \hat{S}_x \omega_1(t) \cos[\phi(t)] + \hat{S}_y \omega_1(t) \sin[\phi(t)] + A_z(t) \hat{S}_z \hat{I}_z \quad (1)$$

where g and A_z are the instantaneous g -tensor value and secular hyperfine coupling; ω_{mw} is the millimeter-wave frequency (in rad per second); ω_1 is the nutation frequency (in rad per second); ϕ is the phase of the millimeter-wave pulse; \hat{S}_z , \hat{S}_y , and \hat{S}_x are the electron spin operators; and \hat{I}_z is the nuclear spin operator. We only considered the secular hyperfine coupling in the simulations here as, under high magnetic field and weak millimeter-wave pulses, the ESEEM effect can be neglected. This Hamiltonian can be projected on the nuclear spin state $m_I \in \{-1, 0, 1\}$ and is thus the sum of three independent ones

$$\hat{H}(t) = \sum_{m_I} \hat{H}_{m_I}(t) = \sum_{m_I} [g(t)\mu_B B_0 - \omega_{\text{mw}} + A_z(t)m_I] \hat{S}_z + \hat{S}_x \omega_1(t) \cos[\phi(t)] + \hat{S}_y \omega_1(t) \sin[\phi(t)] |m_I\rangle \langle m_I| \quad (2)$$

The time evolution of the spin system is obtained from the Liouville von-Neumann equation

$$i\hbar \frac{d\hat{\rho}(t)}{dt} = [\hat{H}(t), \hat{\rho}(t)] \quad (3)$$

This equation can be written in Liouville space to include relaxation. In the basis $\left\{ \hat{E} |m_I\rangle \langle m_I|, \hat{S}_z |m_I\rangle \langle m_I|, \hat{S}_y |m_I\rangle \langle m_I|, \hat{S}_x |m_I\rangle \langle m_I| \right\}$, where \hat{E} is the identity, this leads to the homogeneous Bloch equation, and it is possible to account for T_1 and T_2 relaxation of the spin packets. The density matrix can be written as a linear combination in the basis $\left\{ \hat{E}, \hat{S}_z, \hat{S}_y, \hat{S}_x \right\}$, and the corresponding vector, $\hat{\sigma}$, evolves under a reformulated equation

$$\frac{d\hat{\sigma}(t)}{dt} = \hat{L}(t)\hat{\sigma}(t) = \sum_{m_I} \hat{L}_{m_I}(t)\hat{\sigma}(t) \quad (4)$$

where \hat{L} is the Liouvillian commutation super-operator $[\hat{H}(t), \cdot]$. The Liouvillian consists of three independent blocks, each per m_I subspace. Each corresponding block, $\hat{L}_{m_I}(t) = [\hat{H}_{m_I}(t), \cdot]$ is defined as (51)

$$\hat{L}_{m_I}(t) = \begin{bmatrix} 0 & 0 & 0 & 0 \\ \frac{P_{0,m_I}}{T_1} & -\frac{1}{T_1} & \omega_1(t)\cos[\phi(t)] & -\omega_1(t)\sin[\phi(t)] \\ 0 & -\omega_1(t)\cos[\phi(t)] & -\frac{1}{T_2} & g(t)\mu_B B_0 - \omega_{\text{mw}} + A_z(t)m_I \\ 0 & +\omega_1(t)\sin[\phi(t)] & -g(t)\mu_B B_0 + \omega_{\text{mw}} - A_z(t)m_I & -\frac{1}{T_2} \end{bmatrix} \quad (5)$$

where P_{0,m_I} is the expectation value of $\hat{S}_z |m_I\rangle \langle m_I|$ when the spin system is at thermal equilibrium, $P_{0,m_I} = \text{trace}(\hat{S}_z |m_I\rangle \langle m_I| \hat{\rho}_{\text{eq}})$ where $\hat{\rho}_{\text{eq}}(t) = \exp(-\hat{H}_0 / k_B T)$, and \hat{H}_0 is the same Hamiltonian in the laboratory frame and $T = 293 \text{ K}$. The equation is numerically integrated in a stepwise fashion to obtain

$$\hat{\sigma}(N\delta t) = \prod_{k=0}^N e^{-\hat{L}(t_k)\delta t} \hat{\sigma}(0) \quad (6)$$

The time steps were set to $\delta t = \frac{1}{2^{14} \nu_r}$, where ν_r is the MAS frequency, for the spinning spectra. The echo was integrated from $-0.5 t_{p1}$ to $0.5 t_{p1}$ relative to the nominal echo time: $t_{\text{echo}} = t_{p1} + t_{p2} + 2\tau$; except otherwise noted, $t_{p1} = t_{p2} = 1 \mu\text{s}$; $\tau = 0.7 \mu\text{s}$, $\nu_1 = 200 \text{ kHz}$. A three-angle ZCW grid made of 36,960 points was used for powder averaging (82, 83). The simulations used a T_1 of 1.5 ms and a T_2 of $4 \mu\text{s}$, which are close to the experimental values.

Supplementary Materials

The PDF file includes:

Supplementary Text

Figs. S1 to S4

Legend for data S1

Other Supplementary Material for this manuscript includes the following:

Data S1

REFERENCES AND NOTES

1. J. Krzystek, A. Ozarowski, J. Telsner, Multi-frequency, high-field EPR as a powerful tool to accurately determine zero-field splitting in high-spin transition metal coordination complexes. *Coord. Chem. Rev.* **250**, 2308–2324 (2006).
2. A. Savitsky, K. Möbius, High-field EPR. *Photosynth. Res.* **102**, 311–333 (2009).

3. A. Schnegg, Very-high-frequency EPR. *eMagRes* **6**, 115–132 (2017).
4. J. C. G. Lesurf, *Millimetre-Wave Optics, Devices and Systems* (CRC Press, 2019).
5. P. F. Goldsmith, "Quasioptical system design: Principles and examples" in *Quasioptical Systems* (IEEE, 2009), pp. 331–358.
6. A. F. Gullá, D. E. Budil, Engineering and design concepts for quasioptical high-field electron paramagnetic resonance. *Concepts Magn. Reson. Part B Magn. Reson. Eng.* **22B**, 15–36 (2004).
7. F. Muller, M. A. Hopkins, N. Coron, M. Grynberg, L. C. Brunel, G. Martinez, A high magnetic field EPR spectrometer. *Rev. Sci. Instrum.* **60**, 3681–3684 (1989).
8. A. K. Hassan, A. L. Maniero, H. van Tol, C. Saylor, L.-C. Brunel, High-field EMR: Recent CW developments at 25 tesla, and next-millennium challenges. *Appl. Magn. Reson.* **16**, 299–308 (1999).
9. M. R. Fuchs, T. F. Prisner, K. Möbius, A high-field/high-frequency heterodyne induction-mode electron paramagnetic resonance spectrometer operating at 360 GHz. *Rev. Sci. Instrum.* **70**, 3681–3683 (1999).
10. H. Blok, J. A. J. M. Disselhorst, S. B. Orlinskii, J. Schmidt, A continuous-wave and pulsed electron spin resonance spectrometer operating at 275 GHz. *J. Magn. Reson.* **166**, 92–99 (2004).
11. K. A. Earle, B. Dzikovski, W. Hofbauer, J. K. Moscicki, J. H. Freed, High-frequency ESR at ACERT. *Magn. Reson. Chem.* **43**, S256–S266 (2005).
12. G. M. Smith, J. C. G. Lesurf, R. H. Mitchell, P. C. Riedi, Quasi-optical cw mm-wave electron spin resonance spectrometer. *Rev. Sci. Instrum.* **69**, 3924–3937 (1998).
13. M. Rohrer, O. Brüggemann, B. Kinzer, T. F. Prisner, High-field/high-frequency EPR spectrometer operating in pulsed and continuous-wave mode at 180 GHz. *Appl. Magn. Reson.* **21**, 257–274 (2001).
14. E. Reijerse, P. P. Schmidt, G. Klihm, W. Lubitz, A CW and pulse EPR spectrometer operating at 122 and 244 GHz using a quasi-optical bridge and a cryogen-free 12 T superconducting magnet. *Appl. Magn. Reson.* **31**, 611–626 (2007).
15. T. Dubroca, X. Wang, F. Mentink-Vigier, B. Trociewitz, M. Starck, D. Parker, M. S. Sherwin, S. Hill, J. Krzystek, Terahertz EPR spectroscopy using a 36-tesla high-homogeneity series-connected hybrid magnet. *J. Magn. Reson.* **353**, 107480 (2023).
16. S. Takahashi, L.-C. Brunel, D. T. Edwards, J. van Tol, G. Ramian, S. Han, M. S. Sherwin, Pulsed electron paramagnetic resonance spectroscopy powered by a free-electron laser. *Nature* **489**, 409–413 (2012).
17. K. A. Earle, D. S. Tipikin, J. H. Freed, Far-infrared electron-paramagnetic-resonance spectrometer utilizing a quasioptical reflection bridge. *Rev. Sci. Instrum.* **67**, 2502–2513 (1996).
18. G. W. Morley, L.-C. Brunel, J. van Tol, A multifrequency high-field pulsed electron paramagnetic resonance/electron-nuclear double resonance spectrometer. *Rev. Sci. Instrum.* **79**, 064703 (2008).
19. A. L. Barra, High- and multi-frequency EPR study of Mn12: A new technique for studying new objects. *Inorganica Chim. Acta* **361**, 3564–3569 (2008).
20. O. Laguta, M. Tuček, J. Van Slageren, P. Neugebauer, Multi-frequency rapid-scan HF-EPR. *J. Magn. Reson.* **296**, 138–142 (2018).
21. A. S. Lilly Thankamony, J. J. Wittmann, M. Kaushik, B. Corzilius, Dynamic nuclear polarization for sensitivity enhancement in modern solid-state NMR. *Prog. Nucl. Magn. Reson. Spectrosc.* **102**, 120–195 (2017).
22. C. F. Hwang, D. A. Hill, Phenomenological model for the new effect in dynamic polarization. *Phys. Rev. Lett.* **19**, 1011–1014 (1967).
23. T. R. Carver, C. P. Slichter, Experimental verification of the overhauser nuclear polarization effect. *Phys. Rev.* **102**, 975–980 (1956).
24. A. W. Overhauser, Polarization of nuclei in metals. *Phys. Rev.* **92**, 411–415 (1953).
25. T. V. Can, Q. Z. Ni, R. G. Griffin, Mechanisms of dynamic nuclear polarization in insulating solids. *J. Magn. Reson.* **253**, 23–35 (2015).
26. K. Kundu, F. Mentink-Vigier, A. Feintuch, S. Vega, DNP mechanisms. *eMagRes* **8**, 295–338 (2019).
27. Y. Hovav, I. Kaminker, D. Shimon, A. Feintuch, D. Goldfarb, S. Vega, The electron depolarization during dynamic nuclear polarization: Measurements and simulations. *Phys. Chem. Chem. Phys.* **17**, 226–244 (2015).
28. A. Leavesley, D. Shimon, T. Ann Siaw, A. Feintuch, D. Goldfarb, S. Vega, I. Kaminker, S. Han, Effect of electron spectral diffusion on static dynamic nuclear polarization at 7 Tesla. *Phys. Chem. Chem. Phys.* **19**, 3596–3605 (2017).
29. I. Kaminker, S. Han, Amplification of dynamic nuclear polarization at 200 GHz by arbitrary pulse shaping of the electron spin saturation profile. *J. Phys. Chem. Lett.* **9**, 3110–3115 (2018).
30. D. Shimon, I. Kaminker, A transition from solid effect to indirect cross effect with broadband microwave irradiation. *Phys. Chem. Chem. Phys.* **24**, 7311–7322 (2022).
31. Y. Matsuki, T. Fujiwara, Cryogenic platforms and optimized DNP sensitivity. *eMagRes* **7**, 16 (2018).
32. A. Lund, G. Casano, G. Menzildjian, M. Kaushik, G. Stevanato, M. Yulikov, R. Jabbour, D. Wissler, M. Renom-Carrasco, C. Thieuleux, F. Bernada, H. Karoui, D. Siri, M. Rosay, I. V. Sergeev, D. Gajan, M. Lelli, L. Emsley, O. Ouari, A. Lesage, TinyPols: A family of water-soluble binitroxides tailored for dynamic nuclear polarization enhanced NMR spectroscopy at 18.8 and 21.1 T. *Chem. Sci.* **11**, 2810–2818 (2020).
33. A. Zaghdoun, G. Casano, O. Ouari, M. Schwarzwälder, A. J. Rossini, F. Aussenac, M. Yulikov, G. Jeschke, C. Copéret, A. Lesage, P. Tordo, L. Emsley, Large molecular weight nitroxide biradicals providing efficient dynamic nuclear polarization at temperatures up to 200 K. *J. Am. Chem. Soc.* **135**, 12790–12797 (2013).
34. K. Thurber, R. Tycko, Low-temperature dynamic nuclear polarization with helium-cooled samples and nitrogen-driven magic-angle spinning. *J. Magn. Reson.* **264**, 99–106 (2016).
35. S. Hediger, D. Lee, F. Mentink-Vigier, G. De Paëpe, MAS-DNP enhancements: hyperpolarization, depolarization, and absolute sensitivity. *eMagRes* **7**, 105–116 (2018).
36. A. Lund, A. Equbal, S. Han, Tuning nuclear depolarization under MAS by electron T_{1e} . *Phys. Chem. Chem. Phys.* **20**, 23976–23987 (2018).
37. A. Henstra, P. Dirksen, J. Schmidt, W. T. Wenckebach, Nuclear spin orientation via electron spin locking (NOVEL). *J. Magn. Reson.* **77**, 389–393 (1988).
38. S. K. Jain, G. Mathies, R. G. Griffin, Off-resonance NOVEL. *J. Chem. Phys.* **147**, 164201 (2017).
39. K. O. Tan, C. Yang, R. T. Weber, G. Mathies, R. G. Griffin, Time-optimized pulsed dynamic nuclear polarization. *Sci. Adv.* **5**, eaav6909 (2019).
40. V. S. Redrouthu, G. Mathies, Efficient pulsed dynamic nuclear polarization with the X-inverse-X sequence. *J. Am. Chem. Soc.* **144**, 1513–1516 (2022).
41. Y. Hovav, D. Shimon, I. Kaminker, A. Feintuch, D. Goldfarb, S. Vega, Effects of the electron polarization on dynamic nuclear polarization in solids. *Phys. Chem. Chem. Phys.* **17**, 6053–6065 (2015).
42. S. K. Jain, T. A. Siaw, A. Equbal, C. B. Wilson, I. Kaminker, S. Han, Reversal of paramagnetic effects by electron spin saturation. *J. Phys. Chem. C* **122**, 5578–5589 (2018).
43. A. Equbal, Y. Li, A. Leavesley, S. Huang, S. Rajca, A. Rajca, S. Han, Truncated cross effect dynamic nuclear polarization: An overhauser effect doppelgänger. *J. Phys. Chem. Lett.* **9**, 2175–2180 (2018).
44. M.-T. Türke, I. Tkach, M. Reese, P. Höfer, M. Bennati, Optimization of dynamic nuclear polarization experiments in aqueous solution at 15 MHz/9.7 GHz: A comparative study with DNP at 140 MHz/94 GHz. *Phys. Chem. Chem. Phys.* **12**, 5893–5901 (2010).
45. A. A. Kuzhelev, D. Dai, V. Denysenkov, I. A. Kirilyuk, E. G. Bagryanskaya, T. F. Prisner, Influence of rotational motion of nitroxides on overhauser dynamic nuclear polarization: A systematic study at high magnetic fields. *J. Phys. Chem. C* **125**, 25651–25659 (2021).
46. B. Reif, S. E. Ashbrook, L. Emsley, M. Hong, Solid-state NMR spectroscopy. *Nat. Rev. Methods Primer* **1**, 2 (2021).
47. M. J. Duer, Ed., *Introduction to Solid-State NMR Spectroscopy* (Wiley-Blackwell, 2004).
48. F. Mentink-Vigier, Ü. Akbey, Y. Hovav, S. Vega, H. Oschkinat, A. Feintuch, Fast passage dynamic nuclear polarization on rotating solids. *J. Magn. Reson.* **224**, 13–21 (2012).
49. K. R. Thurber, R. Tycko, Theory for cross effect dynamic nuclear polarization under magic-angle spinning in solid state nuclear magnetic resonance: The importance of level crossings. *J. Chem. Phys.* **137**, 084508 (2012).
50. K. R. Thurber, R. Tycko, Perturbation of nuclear spin polarizations in solid state NMR of nitroxide-doped samples by magic-angle spinning without microwaves. *J. Chem. Phys.* **140**, 184201 (2014).
51. F. Mentink-Vigier, S. Vega, G. D. Paëpe, Fast and accurate MAS-DNP simulations of large spin ensembles. *Phys. Chem. Chem. Phys.* **19**, 3506–3522 (2017).
52. F. Mentink-Vigier, I. Marin-Montesinos, A. P. Jagtap, T. Halbritter, J. van Tol, S. Hediger, D. Lee, S. T. Sigurdsson, G. De Paëpe, Computationally assisted design of polarizing agents for dynamic nuclear polarization enhanced NMR: The AsymPol Family. *J. Am. Chem. Soc.* **140**, 11013–11019 (2018).
53. M. Hubrich, C. Bauer, H. W. Spiess, Magic-angle spinning electron paramagnetic resonance spectroscopy. *Chem. Phys. Lett.* **273**, 259–264 (1997).
54. D. Hessinger, C. Bauer, M. Hubrich, G. Jeschke, H.-W. Spiess, Magic-angle sample spinning electron paramagnetic resonance—Instrumentation, performance, and limitations. *J. Magn. Reson.* **147**, 217–225 (2000).
55. G. A. Sierra, A. Schweiger, Right-angle sample spinning electron spin resonance. *Rev. Sci. Instrum.* **68**, 1316–1323 (1997).
56. G. A. Sierra, M. A. Schuler, A. Schweiger, Right-angle spinning for sensitivity improvement in pulse EPR experiments. *Chem. Phys. Lett.* **303**, 475–481 (1999).
57. D. Hessinger, C. Bauer, G. Jeschke, H. W. Spiess, Fast right-angle spinning EPR on organic radicals: Resolution enhancement and angle determination. *Appl. Magn. Reson.* **20**, 17–33 (2001).
58. E. P. Saliba, A. B. Barnes, Fast electron paramagnetic resonance magic angle spinning simulations using analytical powder averaging techniques. *J. Chem. Phys.* **151**, 114107 (2019).
59. A. M. Carroll, "Development of a combined DNP/EPR spectrometer for the investigation of small volume samples by solid state NMR," thesis, Yale University, New Haven, CT (2018).
60. K. K. Andersson, P. P. Schmidt, B. Katterle, K. R. Strand, A. E. Palmer, S.-K. Lee, E. I. Solomon, A. Gräslund, A.-L. Barra, Examples of high-frequency EPR studies in bioinorganic chemistry. *J. Biol. Inorg. Chem.* **8**, 235–247 (2003).

61. P. A. S. Cruickshank, D. R. Bolton, D. A. Robertson, R. I. Hunter, R. J. Wylde, G. M. Smith, A kilowatt pulsed 94 GHz electron paramagnetic resonance spectrometer with high concentration sensitivity, high instantaneous bandwidth, and low dead time. *Rev. Sci. Instrum.* **80**, 103102 (2009).
62. O. Nir-Arad, D. H. Shlomi, A. Israelstam, T. Amit, N. Manukovsky, A. B. Fialkov, I. Kaminker, The CW-EPR capabilities of a dual DNP/EPR spectrometer operating at 14 and 7 T. *J. Magn. Reson.* **360**, 107635 (2024).
63. O. Nir-Arad, D. H. Shlomi, N. Manukovsky, E. Laster, I. Kaminker, Nitrogen substitutions aggregation and clustering in diamonds as revealed by high-field electron paramagnetic resonance. *J. Am. Chem. Soc.* **146**, 5100–5107 (2024).
64. P. Chen, B. J. Albert, C. Gao, N. Alaniva, L. E. Price, F. J. Scott, E. P. Saliba, E. L. Sesti, P. T. Judge, E. W. Fisher, A. B. Barnes, Magic angle spinning spheres. *Sci. Adv.* **4**, eaau1540 (2018).
65. C. Gao, P. T. Judge, E. L. Sesti, L. E. Price, N. Alaniva, E. P. Saliba, B. J. Albert, N. J. Soper, P.-H. Chen, A. B. Barnes, Four millimeter spherical rotors spinning at 28 kHz with double-saddle coils for cross polarization NMR. *J. Magn. Reson.* **303**, 1–6 (2019).
66. T. M. Osborn Popp, A. Däpp, C. Gao, P.-H. Chen, L. E. Price, N. H. Alaniva, A. B. Barnes, Highly stable magic angle spinning spherical rotors lacking turbine grooves. *Magn. Reson.* **1**, 97–103 (2020).
67. L. E. Price, N. Alaniva, M. Millen, T. Epprecht, M. A. Urban, A. Däpp, A. B. Barnes, Cryogenic-compatible spherical rotors and stators for magic angle spinning dynamic nuclear polarization. *Magn. Reson.* **4**, 231–241 (2023).
68. G. Li, B. Dastrup, R. S. Palani, M. A. Shapiro, S. K. Jawla, R. G. Griffin, K. A. Nelson, R. J. Temkin, Design and optimization of THz coupling in zirconia MAS rotors for dynamic nuclear polarization NMR. *J. Magn. Reson.* **364**, 107722 (2024).
69. K. R. Thurber, A. Potapov, W.-M. Yau, R. Tycko, Solid state nuclear magnetic resonance with magic-angle spinning and dynamic nuclear polarization below 25K. *J. Magn. Reson.* **226**, 100–106 (2013).
70. F. J. Scott, T. Dubroca, R. W. Schurko, S. Hill, J. Long, F. Mentink-Vigier, Characterization of dielectric properties and their impact on MAS-DNP NMR applications. *J. Magn. Reson.*, 107742 (2024).
71. A. Cox, M. E. Newton, J. M. Baker, ¹³C, ¹⁴N and ¹⁵N ENDOR measurements on the single substitutional nitrogen centre (P1) in diamond. *J. Phys. Condens. Matter* **6**, 551–563 (1994).
72. E. L. Hahn, Spin echoes. *Phys. Rev.* **80**, 580–594 (1950).
73. S. Bussandri, D. Shimon, A. Equbal, Y. Ren, S. Takahashi, C. Ramanathan, S. Han, P1 center electron spin clusters are prevalent in type Ib diamonds. *J. Am. Chem. Soc.* **146**, 5088–5099 (2024).
74. G. A. Sierra, A. Schweiger, Anisotropy-resolved electron paramagnetic resonance spectroscopy. *Mol. Phys.* **95**, 973–987 (1998).
75. I. Kaminker, M. Florent, B. Epel, D. Goldfarb, Simultaneous acquisition of pulse EPR orientation selective spectra. *J. Magn. Reson.* **208**, 95–102 (2011).
76. E. A. Nanni, A. B. Barnes, Y. Matsuki, P. P. Woskov, B. Corzilius, R. G. Griffin, R. J. Temkin, Microwave field distribution in a magic angle spinning dynamic nuclear polarization NMR probe. *J. Magn. Reson.* **210**, 16–23 (2011).
77. D. E. M. Hoff, B. J. Albert, E. P. Saliba, F. J. Scott, E. J. Choi, M. Mardini, A. B. Barnes, Frequency swept microwaves for hyperfine decoupling and time domain dynamic nuclear polarization. *Solid State Nucl. Magn. Reson.* **72**, 79–89 (2015).
78. A. Porea, C. Reiter, A. I. Dimitriadis, E. de Rijk, F. Aussenac, I. Sergeyev, M. Rosay, F. Engelke, Improved waveguide coupling for 1.3 mm MAS DNP probes at 263 GHz. *J. Magn. Reson.* **302**, 43–49 (2019).
79. Z. Gan, High-resolution chemical shift and chemical shift anisotropy correlation in solids using slow magic angle spinning. *J. Am. Chem. Soc.* **114**, 8307–8309 (1992).
80. D. Goldfarb, Y. Lipkin, A. Potapov, Y. Gorodetsky, B. Epel, A. M. Raitisimring, M. Radoul, I. Kaminker, HYSCORE and DEER with an upgraded 95 GHz pulse EPR spectrometer. *J. Magn. Reson.* **194**, 8–15 (2008).
81. A. A. Nevzorov, A. Marek, S. Milikisiyants, A. I. Smirnov, High-frequency high-power DNP/EPR spectrometer operating at 7 T magnetic field. *J. Magn. Reson.* **362**, 107677 (2024).
82. H. Conroy, Molecular Schrödinger equation. VIII. A new method for the evaluation of multidimensional integrals. *J. Chem. Phys.* **47**, 5307–5318 (1967).
83. S. K. Zaremba, Good lattice points, discrepancy, and numerical integration. *Ann. Mat. Pura Ed Appl.* **73**, 293–317 (1966).

Acknowledgments: We thank the mechanical workshop team at Tel-Aviv University for the design and construction of various parts. **Funding:** I.K. acknowledges support from the Israel Science Foundation (grant nos. 2149/19 and 1058/23). O.N.A. is a fellow of the Ariane de Rothschild Women's Doctoral Program. The National High Magnetic Field Laboratory (NHMFL) is funded by the National Science Foundation Division of Materials Research (DMR-1644779 and DMR-2128556) and the State of Florida. A portion of this work was supported by National Institutes of Health grant RM1-GM148766 to F.M.V. **Author contributions:** Hardware development: A.B.F., D.H.S., and I.K. Experiments: O.N.A., A.B.F., and I.K. Simulations: F.M.V. Data analysis: O.N.A., N.M., and I.K. Manuscript preparation: O.N.A., A.B.F., N.M., F.M.V., and I.K. Supervision: I.K. **Competing interests:** The authors declare that they have no competing interests. **Data and materials availability:** All data needed to evaluate the conclusions in the paper are present in the paper and/or the Supplementary Materials.

Submitted 23 May 2024

Accepted 29 July 2024

Published 30 August 2024

10.1126/sciadv.adq6073